Research Square

Preprints are preliminary reports that have not undergone peer review.
They should not be considered conclusive, used to inform clinical practice,
or referenced by the media as validated information.

# Plasticity-based topology optimization using weak-form lower-bound yield design and displacement finite elements

**Canh V. Le**

canhlv@hcmute.edu.vn

Ho Chi Minh City University of Technology and Engineering

**Dong Qian**

The University of Texas at Dallas

**Hung Nguyen-Xuan**

VinUniversity

**Research Article**

**Keywords:**

**Posted Date:** November 20th, 2026

**DOI:** https://doi.org/10.21203/rs.3.rs-11584818/v1

**License:** This work is licensed under a Creative Commons Attribution 4.0 International License.
Read Full License

**Additional Declarations:** No competing interests reported.

**EC manuscript No.**
(will be inserted by the editor)

# Plasticity-based topology optimization using weak-form lower-bound yield design and displacement finite elements

**Canh V. Le · Dong Qian · H. Nguyen-Xuan**

Received: date / Accepted: date

**Abstract** This paper presents a topology optimization framework based on weak-form lower-bound yield design and second-order cone programming (SOCP) for the design of structures under plastic admissibility constraints. The proposed method integrates weak-form lower-bound plastic yield design with density-based topology optimization through a sequential convex optimization strategy, in which material density variables, residual stress equilibrium, and plastic admissibility constraints are incorporated into second-order cone programming (SOCP) sub-problems. The structural topology is represented by an element-wise density field, while the stress field is decomposed into elastic and residual components to satisfy equilibrium and yield conditions. An exponential penalization strategy is introduced to suppress intermediate densities and promote clear black-and-white topologies. Unlike many existing stress- or mixed-based formulations, the proposed framework employs conventional displacement-based finite elements, thereby simplifying implementation and avoiding the additional complexity associated with stress- or mixed-based finite element discretizations. Finite element discretization combined with density filtering is employed to improve numerical stability and reduce mesh dependence in the optimized solutions. Several benchmark problems are investigated to demonstrate the effectiveness and robustness of the proposed method. The numerical results show that the proposed approach successfully captures physically meaningful load-transfer mechanisms, generates clear structural layouts, and produces stress distributions consistent with the plastic admissibility condition.

Canh V. Le
Faculty of Civil Engineering, Ho Chi Minh City University of Technology and Engineering, Viet Nam
E-mail: canhlv@hcmute.edu.vn

Dong Qian
Department of Mechanical Engineering, The University of Texas at Dallas, Richardson, TX, 75080, USA

H. Nguyen-Xuan
Center for AI Research, VinUniversity, Ho Chi Minh City, Vietnam

**Keywords** Plastic-based topology optimization · exponential penalization · optimized structural layout · Conic programming

## 1 Introduction

Topology optimization has emerged as a powerful computational design methodology for obtaining efficient structural layouts within a prescribed design domain. By optimally distributing material according to specified objective functions and constraints, topology optimization enables the automatic generation of lightweight, high-performance, and mechanically efficient structures. Over the past decades, topology optimization has been extensively applied in structural mechanics, aerospace, automotive, and civil engineering applications (Hoang and Nguyen-Xuan, 2026; Wang et al., 2023, 2021; Xia and Breitkopf, 2017; Bendsøe and Sigmund, 2004; Eschenauer and Olhoff, 2001; Hassani and Hinton, 1999)

Despite these advances, most continuum topology optimization studies have focused primarily on linear elastic material behavior. However, purely elastic formulations may be insufficient for accurately predicting structural performance near collapse or under severe loading conditions that involve material yielding and irreversible deformations. To overcome these limitations, stress-constrained topology optimization approaches have been developed to incorporate local stress constraints and material failure considerations into the design process (Duysinx and Bendsøe, 1998; Bruggi, 2008; Le et al., 2010; Luo and Kang, 2012; Luo et al., 2013; Xu et al., 2021; Kundu and Zhang, 2023; Cheng et al., 2024). One of the main challenges in conventional stress-constrained topology optimization is the treatment of numerous local stress constraints, which are generally nonlinear functions of the design variables through the structural equilibrium equations. This introduces considerable computational difficulties, particularly in sensitivity analysis and the treatment of stress singularities at near-zero densities. Furthermore, these methods generally rely on stress fields obtained from linear elastic analyses and therefore do not directly account for plastic load redistribution and collapse behavior. In contrast, fully nonlinear elasto-plastic computations incorporated into the topology optimization process can directly account for material yielding and collapse behavior (Maute et al., 1998; Amir, 2017; Li et al., 2017; Kuci and Jansen, 2022; Alcazar et al., 2025). They enable optimization of the structural load-bearing capacity. However, elasto-plastic analyses require incremental–iterative nonlinear computations with repeated equilibrium updates and constitutive integrations. Each design iteration typically involves multiple load increments, with several nonlinear equilibrium iterations and constitutive updates required at each increment. Consequently, the computational effort increases with both the number of load increments and the nonlinear iterations needed for convergence. They lead to significantly greater computational expense. In addition, the implementation of elastoplastic topology optimization is considerably more complicated due to the nonlinear constitutive formulations and the sensitivity analysis associated with path-dependent material behavior.

Based on yield design theory, the load-bearing capacity is evaluated by determining the maximum load

factor for which an admissible internal stress field exists that equilibrates the applied loading while satisfying the material strength criterion throughout the structural domain. Analogously, topology optimization aims to determine the optimal material distribution within a prescribed design domain such that the structure can sustain the applied loads while satisfying strength and performance requirements with minimum material usage. Consequently, the integration of yield design and topology optimization has led to the development of yield design-based topology optimization methods, which directly optimize structural load-bearing capacity and collapse resistance. Compared with conventional elasto-plastic topology optimization, these approaches avoid incremental nonlinear analyses and repeated constitutive updates by evaluating plastic admissibility directly. However, their overall computational efficiency depends on the size and complexity of the resulting optimization problems. One of the earliest contributions to yield design-based topology optimization was the work of Kammoun and Smaoui (2014), who incorporated static and plastic admissibility conditions into a finite-element framework for plane strain structures with Tresca yield behavior. Subsequently, Herfelt et al. (2019) introduced a convex strength-based topology optimization formulation for isotropic von Mises materials using stress-based finite elements, while Mourad et al. (2021) further developed a convex framework for maximizing structural load-bearing capacity under material strength and volume constraints. More recently, Zhang et al. (2023) proposed a plasticity-based topology optimization framework combining mixed finite elements and density-based topology optimization within an efficient SOCP formulation.

Motivated by these developments, this paper presents a topology optimization framework based on weak-form lower-bound yield design and second-order cone programming (SOCP) for the design of structures under plastic admissibility constraints. The key contribution of the proposed work lies in the integration of weak-form lower-bound plastic yield design with density-based topology optimization through a sequential convex optimization strategy. Unlike many existing stress- or mixed-based formulations, the proposed approach employs conventional displacement-based finite elements, allowing elastic reference stresses to be computed using standard finite element procedures without requiring specialized stress interpolation or mixed discretizations. Residual stress equilibrium is instead enforced in a weak form, providing a practical alternative that facilitates integration with existing displacement-based finite element codes while retaining a convex SOCP structure for each optimization subproblem. In the proposed formulation, the structural topology is described by an element-wise density field, while the stress field is decomposed into elastic and residual components to satisfy equilibrium and yield conditions. Although element-wise plastic admissibility constraints are retained, they are expressed as second-order cone constraints by treating residual stresses as independent optimization variables. For fixed elastic reference stresses and penalization coefficients, the resulting optimization subproblems are convex and do not require explicit evaluation of stress sensitivities with respect to the design variables. Thus, the princi-

pal computational advantage lies in the mathematical treatment of local constraints rather than their elimination or reduction in number. An exponential penalization strategy (Smaoui and Kammoun, 2022; Zhang et al., 2023) is introduced to suppress intermediate densities and promote clear black-and-white topologies. The plasticity-based topology optimization problem is then solved through a sequence of second-order cone programs, enabling the use of primal-dual interior-point algorithms. Furthermore, finite element discretization combined with density filtering is adopted to improve numerical stability, suppress checkerboard patterns and reduce mesh sensitivity. Several benchmark examples, including the double-clamped beam, L-bracket, and bridge design, are conducted to demonstrate the effectiveness and robustness of the proposed framework. The numerical results show that the proposed framework successfully captures physically meaningful load-transfer mechanisms, generates clear structural layouts, and produces stress distributions consistent with the plastic admissibility condition.

## 2 Numerical weak-form lower-bound yield design

Consider a 2D structure occupying domain $\Omega \subset \mathbb{R}^2$ with boundary $\partial\Omega = \Gamma_u \cup \Gamma_t$. The structure is subjected to external traction $\mathbf{t}$ on $\Gamma_t$ and displacement constraints on $\Gamma_u$. In yield design, the goal is to determine the maximum load factor $\lambda$ for which the stress field satisfies equilibrium and the material yield condition. Throughout this section, Voigt notation is adopted for the plane-stress formulation. The stress and strain vectors are defined as $\boldsymbol{\sigma} = [\sigma_{xx}, \sigma_{yy}, \tau_{xy}]^T$ and $\boldsymbol{\varepsilon} = [\varepsilon_{xx}, \varepsilon_{yy}, \gamma_{xy}]^T$, respectively, where $\gamma_{xy} = 2\varepsilon_{xy}$ is the engineering shear strain. The total stress field is decomposed as

$$\boldsymbol{\sigma} = \lambda \boldsymbol{\sigma}^E + \boldsymbol{\sigma}_r \tag{1}$$

where $\lambda$ is the load factor, $\boldsymbol{\sigma}^E$ denotes the fictitious elastic stress field obtained from an auxiliary linear elastic analysis under the prescribed reference loading, and $\boldsymbol{\sigma}_r$ is the residual stress field. The fictitious elastic stress field serves as a reference for constructing a plastically admissible total stress field and does not represent the actual material state at collapse.

Since $\boldsymbol{\sigma}^E$ equilibrates the prescribed reference loading, the residual stress field $\boldsymbol{\sigma}_r$ must be self-equilibrated

$$\mathbf{L}^T \boldsymbol{\sigma}_r = \mathbf{0} \tag{2}$$

where $\mathbf{L}$ is the strain–displacement differential operator, defined for plane problems as

$$\mathbf{L} = \begin{bmatrix} \partial/\partial x & 0 \\ 0 & \partial/\partial y \\ \partial/\partial y & \partial/\partial x \end{bmatrix} \tag{3}$$

where $\mathbf{L}^T$ represents the corresponding equilibrium differential operator.

Instead of enforcing the above strong form, the corresponding weak form is employed. For any kinematically admissible virtual displacement field $\delta\mathbf{u}$ satisfying $\delta\mathbf{u} = \mathbf{0}$ on $\Gamma_u$, the residual stress equilibrium condition

is

$$\int_{\Omega} \boldsymbol{\sigma}_r^T \delta\boldsymbol{\varepsilon}\, d\Omega = 0 \tag{4}$$

where

$$\delta\boldsymbol{\varepsilon} = \mathbf{L}\delta\mathbf{u} \tag{5}$$

Using linear triangular finite elements, the virtual strain field is approximated by

$$\delta\boldsymbol{\varepsilon}_e = \mathbf{B}_e \delta\mathbf{u}_e \tag{6}$$

in which $\delta\mathbf{u}_e$ is the vector of element nodal virtual displacements, and $\mathbf{B}_e$ is the element strain–displacement matrix, given by

$$\mathbf{B}_e = \begin{bmatrix} N_{1,x} & 0 & N_{2,x} & 0 & N_{3,x} & 0 \\ 0 & N_{1,y} & 0 & N_{2,y} & 0 & N_{3,y} \\ N_{1,y} & N_{1,x} & N_{2,y} & N_{2,x} & N_{3,y} & N_{3,x} \end{bmatrix} \tag{7}$$

where $N_{i,x}$ and $N_{i,y}$ denote the spatial derivatives of the element shape functions. For the global equilibrium formulation, the element matrix $\mathbf{B}_e$ is subsequently mapped to the global free degrees of freedom, with zero entries at positions not associated with the element. For simplicity, the same notation $\mathbf{B}_e$ is retained for the resulting global strain–displacement matrix in the subsequent equilibrium equations. Although T3 elements are used in this study, the proposed formulation can be extended to higher-order triangular and quadrilateral elements using appropriate strain–displacement matrices and numerical integration.

The weak residual equilibrium becomes

$$\sum_{e=1}^{n_e} \int_{\Omega_e} \delta\mathbf{u}_e^T \mathbf{B}_e^T \boldsymbol{\sigma}_{r,e}\, d\Omega = 0 \tag{8}$$

Because the virtual displacements are arbitrary at all free degrees of freedom, the discrete self-equilibrium equation for the residual stress field is

$$\sum_{e=1}^{n_e} \int_{\Omega_e} \mathbf{B}_e^T \boldsymbol{\sigma}_{r,e}\, d\Omega = \sum_{e=1}^{n_e} A_e \mathbf{B}_e^T \boldsymbol{\sigma}_{r,e} = \mathbf{0} \tag{9}$$

where $A_e$ is the area of element $e$. The residual stress equilibrium condition is enforced in the finite element weak sense rather than pointwise. Consequently, the resulting stress field is not necessarily strictly statically admissible, and the computed collapse multiplier is regarded as a weak-form lower-bound approximation rather than a rigorous lower bound.

Furthermore, the stress field is required to satisfy the yield condition. In this work, the von Mises criterion under plane stress is adopted and formulated as a second-order cone constraint

$$\left\|\mathbf{D}_{VM}\left(\lambda\boldsymbol{\sigma}_e^E + \boldsymbol{\sigma}_{r,e}\right)\right\|_2 \leq \sigma_p \tag{10}$$

where $\sigma_p$ is the yield stress and

$$\mathbf{D}_{VM} = \begin{bmatrix} 1 & -1/2 & 0 \\ 0 & \sqrt{3}/2 & 0 \\ 0 & 0 & \sqrt{3} \end{bmatrix} \tag{11}$$

The matrix $\mathbf{D}_{VM}$ operates on the Voigt stress vector, such that $\|\mathbf{D}_{VM}\boldsymbol{\sigma}_e\|_2$ represents the plane-stress von Mises equivalent stress, where $\|\cdot\|_2$ denotes the Euclidean norm.

Finally, the weak-form lower-bound yield design problem with stress decomposition is written as

$$\begin{aligned} \max_{\lambda,\boldsymbol{\sigma}_r} \quad & \lambda \\ \text{s.t.} \quad & \sum_{e=1}^{n_e} A_e \mathbf{B}_e^T \boldsymbol{\sigma}_{r,e} = \mathbf{0} \\ & \psi(\boldsymbol{\sigma}_e) = \left\| \mathbf{D}_{VM} \left( \lambda \boldsymbol{\sigma}_e^E + \boldsymbol{\sigma}_{r,e} \right) \right\|_2 \leq \sigma_p, \quad e = 1, \ldots, n_e \end{aligned} \tag{12}$$

The first constraint is the weak-form residual stress equilibrium after finite element discretization and applying kinematic boundary conditions, while the second constraint is the plane-stress von Mises yield condition written as second-order cones.

## 3 Extension of yield design to topology optimization

Classical yield design determines the maximum load factor $\lambda$ that a given structure can sustain before plastic collapse, assuming a fixed geometry and material distribution. In contrast, topology optimization seeks the optimal distribution of material within a prescribed design domain. By combining these two frameworks, one aims to determine not only the collapse load but also the optimal material layout that maximizes structural performance under plastic admissibility constraints.

The density-based topology optimization approach is characterized by a material density field $\rho(\mathbf{x}) \in [\rho_{\min}, 1]$, $\mathbf{x} \in \Omega$. The density variable characterizes the local distribution of material, where $\rho_e = 1$ corresponds to solid material, $\rho_e \approx \rho_{\min}$ represents void (or nearly void) regions, and $\rho_{\min} < \rho_e < 1$ denotes intermediate material states.

In numerical yield design-based topology optimization, the density affects the yield capacity of each element. The effective yield stress is defined as

$$\sigma_p^{\text{eff}} = \rho_e \sigma_p \tag{13}$$

Thus, the von Mises yield condition becomes

$$\psi(\boldsymbol{\sigma}_e) \leq \rho_e \sigma_p \tag{14}$$

This formulation ensures that (i) fully solid regions retain their complete plastic strength, (ii) regions with low density possess diminished load-carrying capacity, and (iii) void-like regions retain a small but nonzero load-carrying capacity due to the prescribed minimum density $\rho_{\min}$.

Plasticity-based topology optimization can be formulated as the minimization of the material volume subject to equilibrium constraints and yield conditions, as follows

$$\begin{aligned} \min_{\boldsymbol{\sigma}_r,\rho} \quad & \int_\Omega \rho \, d\Omega \\ \text{s.t.} \quad & \sum_{e=1}^{n_e} A_e \mathbf{B}_e^T \boldsymbol{\sigma}_{r,e} = \mathbf{0} \\ & \left\| \mathbf{D}_{VM} \left( \lambda \boldsymbol{\sigma}_e^E + \boldsymbol{\sigma}_{r,e} \right) \right\|_2 \leq \rho_e \sigma_p, \quad e = 1, \ldots, n_e \\ & \rho_{\min} \leq \rho_e \leq 1 \end{aligned} \tag{15}$$

where $\lambda$ is a prescribed load factor associated with the given external load.

It is important to note that the density variable $\rho$ plays a dual role in the formulation, as it influences both the objective function and the yield constraint. On the

one hand, $\rho$ appears explicitly in the objective function, where it governs the amount and distribution of material within the design domain, typically promoting material reduction while penalizing intermediate densities. On the other hand, $\rho$ directly affects the admissible stress domain through the yield condition, where the effective yield strength is scaled by the density. As a result, regions with lower density exhibit reduced load-carrying capacity, while fully solid regions retain their full plastic strength. This coupling ensures that the optimization process simultaneously accounts for structural efficiency and plastic admissibility. Consequently, the density field not only determines the geometry of the optimized structure but also controls its mechanical response by linking material distribution with stress feasibility.

## 4 Penalization of the density and filtering

### 4.1 Exponential penalization of the density in the objective function

In density-based topology optimization, the objective function is commonly formulated to minimize the total material usage while promoting a clear distinction between solid and void regions. To achieve this, a penalization scheme is introduced to discourage intermediate density values and drive the solution toward a nearly binary distribution.

In the present work, an exponential penalization Smaoui and Kammoun (2022); Zhang et al. (2023) is adopted. The objective function is defined as

$$J(\rho) = \sum_{e=1}^{n_e} \rho_e \, e^{\,p(1-\rho_e)} A_e \tag{16}$$

where $p > 0$ is the penalization parameter.

The exponential function $g(\rho_e) = e^{\,p(1-\rho_e)}$ serves as a weighting factor that increases as the density decreases. The product $\rho_e g(\rho_e)$ therefore exhibits the following properties: (i) for $\rho_e = 1$, one obtains $\rho_e g(\rho_e) = 1$, so fully solid elements contribute normally to the objective; (ii) as $\rho_e \to 0$, $\rho_e g(\rho_e) \to 0$, implying that void regions contribute negligibly to the objective; and (iii) for $0 < \rho_e < 1$, $\rho_e g(\rho_e) > \rho_e$, which introduces a stronger penalization of intermediate densities compared to the linear case. Therefore, the exponential penalization enhances the contrast between solid and void regions and reduces gray areas in the optimized topology.

Unlike the classical SIMP penalization $\rho^p$, the exponential form provides a smooth and strictly positive weighting function. The objective remains well-defined for all $\rho_e \in [\rho_{\min}, 1]$, and its derivative is continuous

$$\frac{\partial J}{\partial \rho_e} = \left[ e^{\,p(1-\rho_e)} - p\rho_e \, e^{\,p(1-\rho_e)} \right] A_e \tag{17}$$

This smoothness is advantageous for numerical optimization, particularly when the objective function is linearized at each iteration. To preserve the convexity of the subproblem (e.g., in an SOCP framework), the nonlinear objective is linearized at iteration $k$:

$$J^{(k)}(\rho) = \sum_{e=1}^{n_e} c_e^{(k)} \rho_e A_e \tag{18}$$

with

$$c_e^{(k)} = g\left(\rho_e^{(k)}\right) = e^{\,p\left(1-\rho_e^{(k)}\right)} \tag{19}$$

The coefficients $c_e^{(k)}$ are held fixed during the solution of the optimization subproblem and updated at each iteration. This leads to a sequence of convex optimization problems that can be efficiently solved while gradually updating the density field.

From a mechanical perspective, the exponential penalization introduces a higher cost to retain low-density material compared to linear formulations. This encourages the optimizer to either remove material entirely or maintain it at full density, leading to clearer structural layouts. At the same time, the formulation remains consistent with plastic admissibility constraints, ensuring that the resulting topology is both mechanically feasible and materially efficient.

Finally, the topology optimization problem based on yield design can be written as:

$$\begin{aligned}
\min_{\rho,\boldsymbol{\sigma}_r} \quad & \sum_{e=1}^{n_e} c_e \rho_e A_e \\
\text{s.t.} \quad & \sum_{e=1}^{n_e} A_e \mathbf{B}_e^T \boldsymbol{\sigma}_{r,e} = \mathbf{0} \\
& \left\| \mathbf{D}_{VM}\left(\lambda \boldsymbol{\sigma}_e^E + \boldsymbol{\sigma}_{r,e}\right) \right\|_2 \le \rho_e \sigma_p, \quad e = 1, \ldots, n_e \\
& \rho_{\min} \le \rho_e \le 1
\end{aligned} \tag{20}$$

## 4.2 Algorithmic procedure

The plasticity-based topology optimization problem (20) is solved using a sequential convex programming strategy, in which the nonlinear objective is linearized and the resulting subproblem is formulated as a second-order cone program (SOCP). At each iteration, the density field is updated which ensures equilibrium and plastic admissibility.

Let $\rho^{(k)}$ denote the density field in iteration $k$. The algorithm proceeds as follows:

1. **Initialization:** Set an initial density field $\rho^{(0)}$, typically $\rho^{(0)} = 1$ and choose parameters $p$, $\rho_{\min}$, tolerance $\varepsilon$ and the maximum number of iterations.
2. **Elastic analysis:** Solve the reference elastic problem $\mathbf{K}_0\mathbf{u}^{(k)} = \mathbf{F}$ and compute the elastic stress of the element $\boldsymbol{\sigma}_e^{E,(k)} = \mathbf{D}_0\mathbf{B}_e\mathbf{u}_e^{(k)}$.
3. **Objective linearization:** Evaluate the coefficients $c_e^{(k)} = e^{\,p(1-\rho_e^{(k)})}$ and construct the linearized objective $J^{(k)}(\rho) = \sum_{e=1}^{n_e} c_e^{(k)} \rho_e A_e$
4. **SOCP subproblem:** Solve the convex optimization problem (20). This step yields updated variables $\rho^{(k+1)}$ and $\boldsymbol{\sigma}_r^{(k+1)}$.
5. **Density filtering:** Apply a spatial filter to the updated density field to avoid numerical instabilities: $\rho^{(k+1)} \leftarrow \widetilde{\rho}^{(k+1)}$.
6. **Convergence check:** Evaluate the change in density and objective:

$$\Delta\rho = \|\rho^{(k+1)} - \rho^{(k)}\|_\infty, \qquad \Delta J = \frac{|J^{(k+1)} - J^{(k)}|}{\max(1, |J^{(k)}|)}. \tag{21}$$

If $\Delta\rho < \varepsilon$ or $\Delta J < \varepsilon$, stop; otherwise, set $k \leftarrow k+1$ and repeat.

It should be noted that density filtering is performed after solving the SOCP subproblem, following Zhang et al. (2023). Although this procedure regularizes the

material distribution, the filtered density field is not guaranteed to strictly satisfy the original plastic admissibility constraints. A rigorous treatment of this issue is left for future investigation.

### 4.3 Density filtering

Density filtering is applied at step (5) of the algorithmic framework to reduce checkerboard patterns and mesh sensitivity. A Gaussian density filter Sigmund (2007); Zhang et al. (2023) is employed at the element level to regularize the material distribution. Details of the filtering procedure are provided in Appendix A.

## 5 Numerical examples

This section presents benchmark problems from the literature, involving different geometries, loading conditions, and boundary constraints, to assess the proposed topology optimization framework based on yield design and SOCP. All problems are formulated under plane stress and discretized using T3 finite elements. The density field is updated iteratively with filtering to ensure numerical stability and suppress checkerboard patterns. The results demonstrate the ability of the method to produce physically consistent load transfer and meaningful structural topologies. All computations were performed on a workstation with an Intel Core i7-13700 processor (2.10 GHz) and 64 GB of RAM.

### 5.1 Double-clamped beam

The first example considers a double-clamped beam, a topology optimization benchmark for assessing the ability of the proposed method to capture load-carrying mechanisms and generate efficient layouts under plastic admissibility (Jahangiry et al., 2021; Zhang et al., 2023). The beam has a total length of 20 m and a height of 5 m, and is subjected to a uniformly distributed vertical load of 383.2 kN applied over a central segment of length 2.5 m on the top boundary. The material follows the von Mises yield criterion under plane stress conditions with $\sigma_p = 300\,\text{kPa}$. Exploiting symmetry, only the right half of the domain ($10 \times 5\,\text{m}^2$) is analyzed, as shown in Figure 1. First, the effect of the penalty

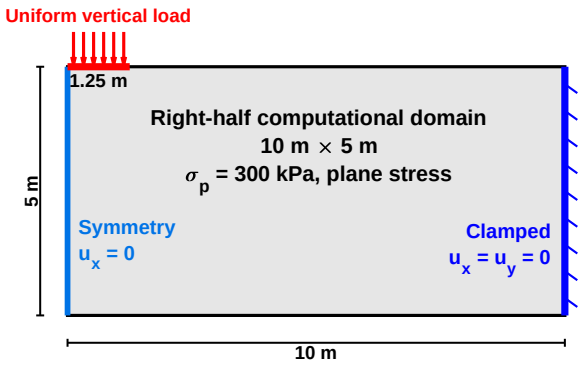



Fig. 1: Double-clamped beam: geometries, loading and computational domain.

parameter $p$ on the material layout is studied for values ranging from 1 to 6 and 10, as shown in Figure 2. Increasing $p$ enhances the penalization of intermediate densities, producing progressively sharper topologies. A well-defined black-and-white layout emerges at $p = 5$, with negligible changes observed for higher values. This indicates that $p \geq 5$ provides sufficient penalization for the proposed method. The final layouts obtained from Zhang et al. (2023) and the proposed method are in good agreement with $p \geq 5$. The corresponding normalized von Mises stress distributions for $p = 3$ and $p = 5$

are also plotted in Figure 2. Based on these observations, $p = 5$ is empirically selected for the subsequent analyses, as it provides a well-defined material layout without requiring further increases in the penalization parameter. This selection is based on qualitative assessment of the resulting topologies rather than a formal quantitative criterion and is not intended to represent a universally optimal value.

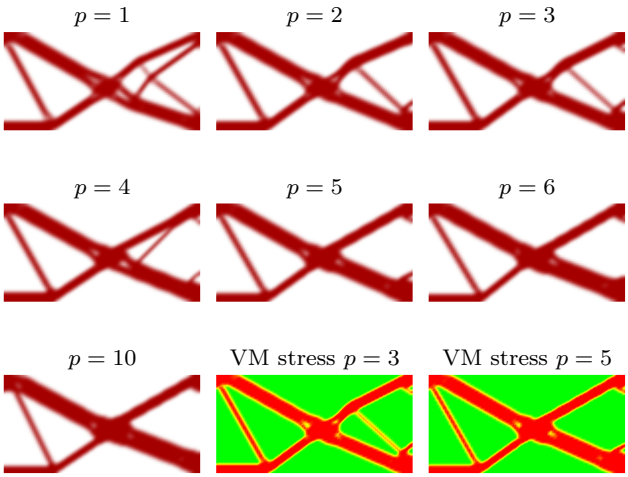



Fig. 2: Double-clamped beam: layouts and von Mises stress from the plasticity-based topology optimization method using different values for $p$.

The convergence history of the proposed topology optimization procedure for $p = 5$ is presented in Figure 3. The evolution of the objective function and the relative objective change with respect to the iteration number demonstrates the convergence behavior of the proposed algorithm. During the early iterations, the objective function decreases rapidly as material is redistributed to satisfy the yield constraints while minimizing the objective function. Subsequently, the rate of change gradually diminishes, indicating that the optimization process approaches a stable solution. The relative objective change, plotted on a logarithmic scale, exhibits non-monotonic fluctuations rather than a consistently decreasing trend. These fluctuations may be associated with the iterative updating of the penalization coefficients. Nevertheless, the objective function approaches a nearly constant value during the later iterations. After 144 iterations, the relative objective change reaches $9.99 \times 10^{-7}$, while the maximum change in element density is $5.56 \times 10^{-5}$, satisfying the prescribed convergence tolerances of $10^{-6}$ and $10^{-4}$, respectively.

The intermediate density distributions shown at different iterations illustrate the progressive formation of the structural topology. At the initial stage (Iter = 1), the material distribution is relatively diffuse, with substantial intermediate-density regions. As the optimization proceeds, inefficient regions are gradually removed and the primary load-transfer paths become clearer. By Iter = 40, the main structural members are already well established, while only minor local modifications occur afterward. The final topology obtained at Iter = 144 exhibits a clear black-and-white distribution with well-defined structural boundaries, demonstrating the effectiveness of the proposed penalization strategy in suppressing intermediate densities and promoting manufacturable designs. It is also observed that the layout at iteration 5 for $p = 5$ closely matches the satisfactory black-and-white design obtained for $p = 4$ at iteration $10^{th}$. This indicates that increasing the penalty parameter accelerates the suppression of intermediate densities and promotes the earlier formation of a well-defined topology, although this does not necessarily imply faster

numerical convergence of the objective function or design variables, while the underlying load-carrying mechanism remains essentially unchanged.

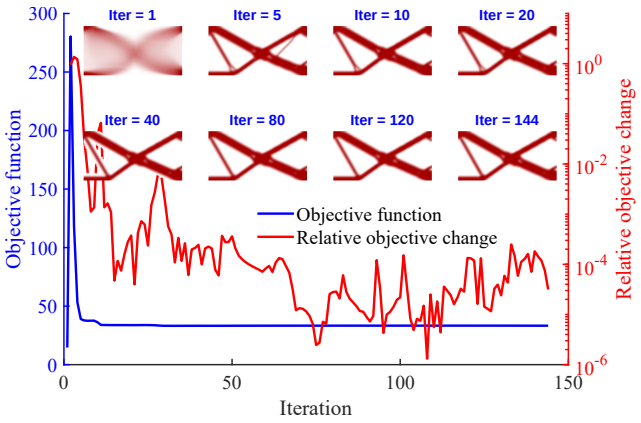



Fig. 3: Double-clamped beam: the evolution of the structural layout, volume and relative error in the optimal design for $p = 5$.

To further assess the mesh sensitivity and computational performance of the proposed formulation, three discretizations with 2,500, 10,000, and 40,000 T3 elements are considered for $p = 5$. The corresponding results are summarized in Table 1. The optimized volume ratios range from 0.3284 to 0.3307, indicating limited sensitivity of the final material volume to mesh refinement. All three discretizations satisfy the prescribed convergence criteria. The total computational time increases with mesh resolution, reflecting both the larger SOCP problems and the greater number of optimization iterations. These results provide a quantitative assessment of the computational performance of the proposed displacement-based formulation without implying superior efficiency relative to existing methods.

To further investigate the influence of the loading position on the optimized topology, an additional computation is performed by relocating the distributed load from the top boundary to the bottom boundary while keeping all other parameters unchanged. This example is used to examine the sensitivity of the proposed method to variations in the load application region and to evaluate the resulting changes in the load-transfer mechanism and structural layout. The optimized layouts obtained for the top-load and bottom-load cases, as shown in Figure 4, exhibit similar global X-shaped load-carrying mechanisms, indicating that the proposed method consistently captures the principal stress-transfer paths under different loading positions. However, changing the load location significantly affects the local material distribution. When the load is applied on the top boundary, the dominant diagonal members develop primarily through the upper part of the structure, whereas loading from the bottom shifts the material concentration toward the lower region. Despite these differences, both cases converge to clear black-and-white topologies with well-defined structural members, demonstrating the robustness of the proposed formulation in generating physically meaningful layouts under varying loading conditions.




Fig. 4: Double-clamped beam: optimized layouts obtained for the top-load and bottom-load cases.

Table 1: Mesh sensitivity and computational performance of the proposed formulation for the double-clamped beam.

| Mesh size (m) | T3 elements | SOCP variables | Iterations | Volume ratio | CPU time (s) |
|---|---|---|---|---|---|
| 0.20 | 2,500 | 20,000 | 66 | 0.3301 | 29.7 |
| 0.10 | 10,000 | 80,000 | 144 | 0.3307 | 266.7 |
| 0.05 | 40,000 | 320,000 | 375 | 0.3284 | 3,405.1 |

### 5.2 L-bracket

The next example considers the L-bracket problem, a widely used benchmark in stress-based topology optimization due to the severe stress concentration induced by the re-entrant corner. The design domain consists of a square plate of size 2.5 m × 2.5 m with a square cut-out of size 1.5 m × 1.5 m removed from the upper-right corner, resulting in an L-shaped geometry. The upper boundary of the left vertical arm is prescribed as a Dirichlet boundary, while a downward distributed load of 10 kN is applied at the middle of the right edge over a segment of length 0.1 m, as shown in Figure 5. This example aims to assess the applicability and numerical robustness of the proposed optimization framework for a geometrically non-convex L-bracket under varying yield stress values, with particular emphasis on the resulting optimal topologies, stress distributions, and convergence behavior.

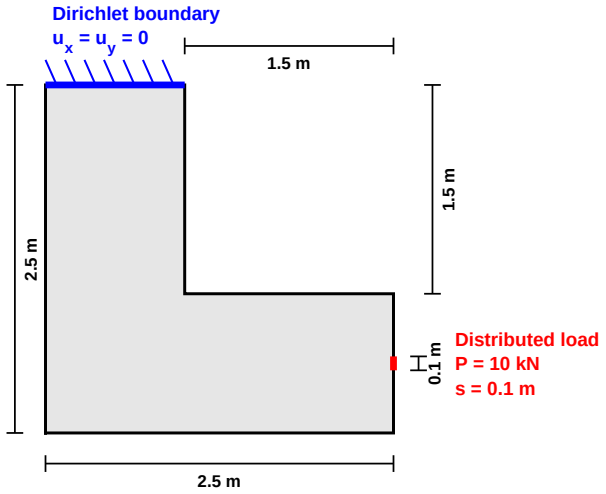



Fig. 5: L-bracket problem: geometries, loading and computational domain.

To investigate the influence of material strength on the optimized topology, a parametric study with respect to the yield stress parameter $\sigma_p$ is conducted. Figure 6 presents the convergence histories and topology evolution of the L-bracket design problem for different yield stress values $\sigma_p = 80,\ 100,\ 120$, and 140 kPa. For all cases, the objective function decreases rapidly during the first few iterations and subsequently approaches a nearly constant value. The relative objective change exhibits non-monotonic fluctuations but generally decreases as the optimization progresses, indicating progressive stabilization of the optimization process.

The intermediate topologies plotted at selected iterations illustrate the progressive redistribution of material from the initial full design toward efficient load-carrying paths. At early iterations, the material distribution remains relatively diffuse with noticeable intermediate densities. As the optimization proceeds, the layouts gradually evolve into clearer black-and-white topologies characterized by distinct truss-like structural members connecting the loading and support regions. Most major structural features become stabilized after approximately 20–40 iterations, while subsequent

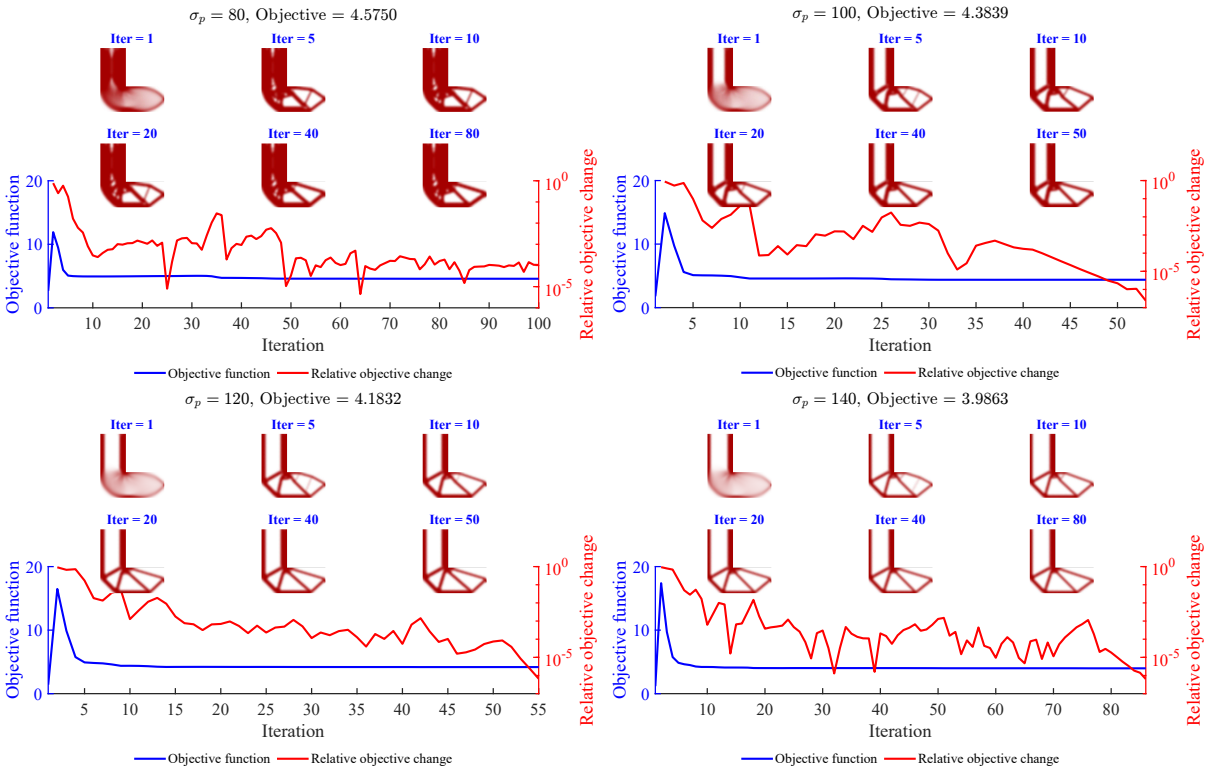



Fig. 6: Convergence histories and topology evolution for different yield stress values of L-bracket problem.

iterations mainly refine local geometric details. The influence of the yield stress parameter on the optimized topology is clearly observed. For lower yield stress values (e.g., $\sigma_p = 80$), thicker and more distributed material regions are required to satisfy the plastic admissibility constraints due to the lower material strength. As $\sigma_p$ increases from 80 to 140, the optimized layouts become progressively thinner and more efficient because stronger materials require less structural volume to resist the applied loading. Consequently, the objective function decreases with increasing yield stress, reflecting the enhanced load-carrying capacity associated with higher material strength.

Figure 7 presents the normalized von Mises stress distributions corresponding to the optimized designs for different yield stress values $\sigma_p = 80,\ 100,\ 120$, and 140. In all cases, the highest stress concentrations occur near the re-entrant corner of the L-bracket, confirming that this region governs the structural response due to the geometric discontinuity and the abrupt change in load-transfer direction. For $\sigma_p = 80$, large yielding regions (shown in red) appear near the vertical arm and the re-entrant corner, indicating extensive yielding and severe stress localization under the low admissible yield stress. As $\sigma_p$ increases to 100, the yielding zones become smoother and align more clearly with the principal load-carrying paths, indicating improved stress redistribution. For $\sigma_p = 120$ and 140, the stress distributions become very similar, with narrower and more organized yielding regions concentrated along the major structural members, while the re-entrant corner remains the dominant yielding region.

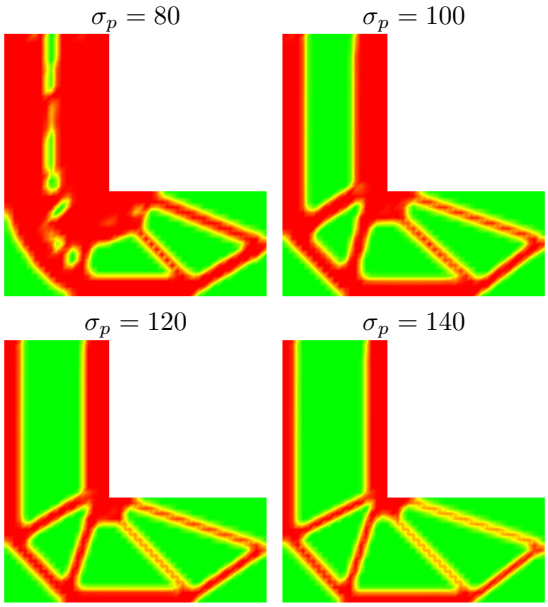



Fig. 7: L-bracket problem: distribution of von Mises stress corresponding to the optimized designs for different yield stress values.

### 5.3 Bridge design problem

The final example considers a bridge design problem previously investigated in Zhang et al. (2023), defined on a rectangular domain of size $180 \times 40\,\mathrm{m}^2$. The bridge is clamped at two bottom supports, each measuring $5 \times 2\,\mathrm{m}^2$, as indicated by the dark gray regions in Figure 8. A uniformly distributed traffic load of $F$ (kPa) is applied along the top surface of the black strip. The strip has a thickness of 1 m and is positioned 25 m below the top boundary and 14 m above the bottom supports. The material yield stress is taken as $\sigma_p = 10\,\mathrm{MPa}$. This example aims to assess the applicability and numerical robustness of the proposed optimization framework for a relatively large-scale bridge structure under varying traffic loads, with particular emphasis on load-dependent optimal topologies, plastic admissibility, and convergence behavior.

To investigate the influence of the external loading magnitude on the optimized topology, a parametric study is conducted for different distributed traffic loads $F$ applied to the bridge structure. The objective is to evaluate the sensitivity of the proposed lower-bound yield design framework to variations in the loading condition and to examine the resulting changes in the structural layout, load-transfer mechanism, stress distribution, and convergence behavior. Figure 9 presents the convergence histories and topology evolution of the bridge problem for traffic loads ranging from $F = 150$ to $F = 300$, using a mesh consisting of 28800 elements and 14661 nodes. For all loading cases, the objective function decreases rapidly during the initial iterations before gradually approaching a nearly constant value. Although the relative objective change exhibits non-monotonic fluctuations, its overall decreasing trend indicates progressive stabilization and satisfactory convergence of the proposed optimization. The optimized layouts are shown in Figure 10. As the traffic load increases, the resulting topologies become progressively denser and develop thicker primary load-carrying members to satisfy the plastic admissibility condition. All optimized designs exhibit clear truss-like load-transfer mechanisms connecting the loading strip to the supports. Moreover, higher load levels lead to stronger reinforcement along the principal diagonal members and a reduction of void regions, reflecting the increased material demand required to sustain larger external loads. The topology evolution histories further demonstrate that the principal structural configuration stabilizes rapidly,

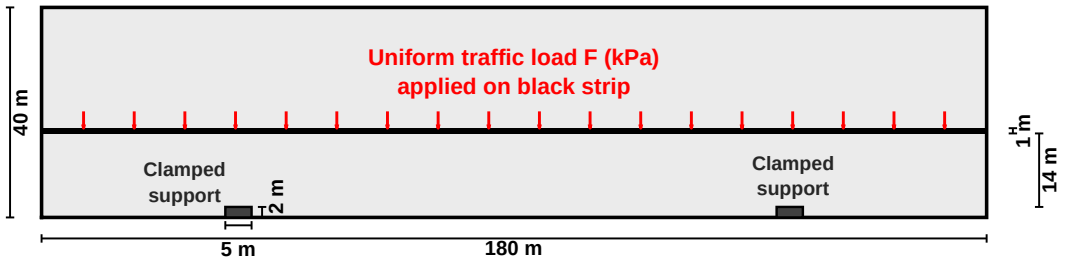



Fig. 8: Bridge problem: geometries, loadings.

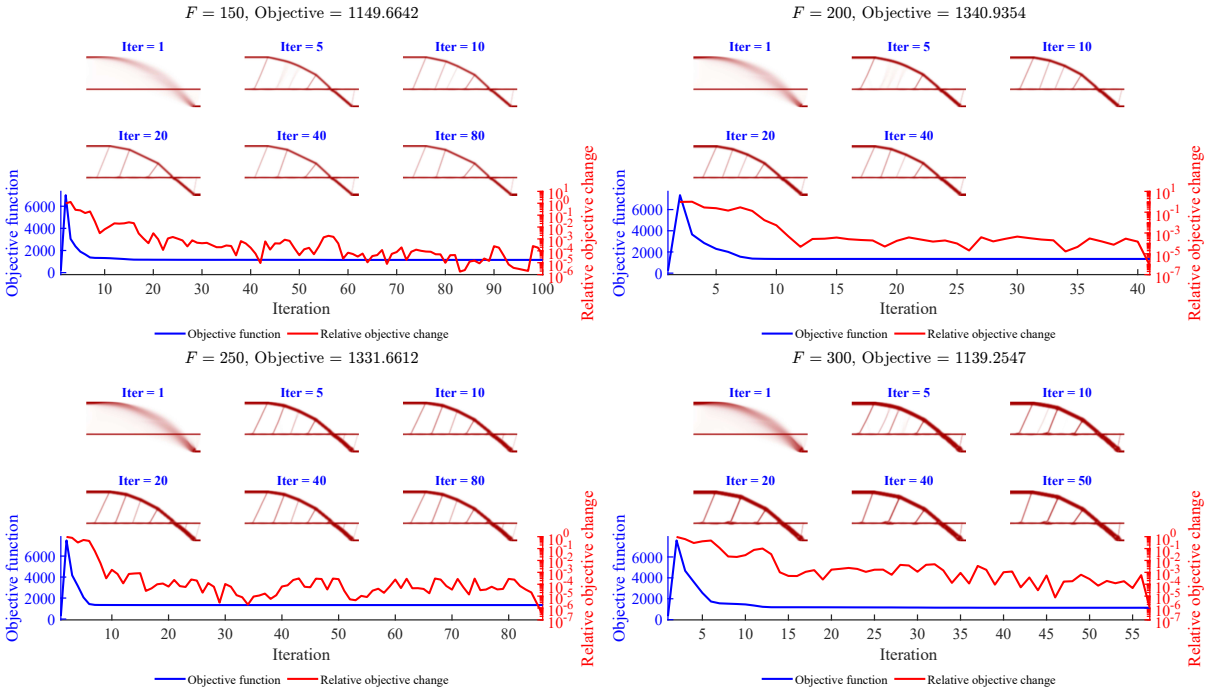



Fig. 9: Bridge problem: convergence histories and topology evolution for different distributed traffic load $F$.

with the dominant load-transfer paths already emerging within the early optimization iterations.

Figure 11 presents the corresponding von Mises stress distributions for the optimized bridge layouts. For all cases, the highest stress values are concentrated along the principal diagonal load-carrying members and near the support regions, confirming that these structural components play a dominant role in transferring the external load. As the traffic load increases, the high-stress regions become more pronounced and extend over larger portions of the primary structural members. Nevertheless, the stress fields remain smooth and well aligned with the truss-like load-transfer mechanisms observed in the optimized topologies. These results demonstrate that the proposed method effectively redistributes stresses throughout the structure while maintaining the plastic admissibility condition under different loading magnitudes.

For $F = 150$, the present result shows good agreement with Zhang et al. (2023) in terms of the overall load-transfer mechanism and the dominant truss-like topology. Both layouts develop three inclined struc-

tural members connecting the lower and upper load-carrying paths. Minor differences can be observed in the locations and orientations of these inclined members, which are likely associated with differences in mesh discretization and implementation details. Nevertheless, the overall structural configuration and the principal load-transfer mechanism remain consistent between the two solutions.

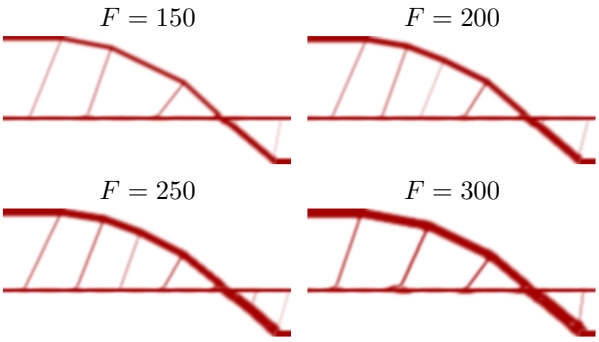



Fig. 10: Bridge problem: layouts corresponding to the optimized designs for different distributed traffic load $F$

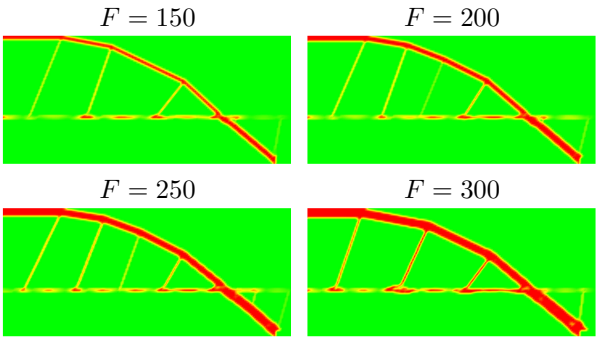



Fig. 11: Bridge problem: distribution of von Mises stress corresponding to the optimized designs for different distributed traffic load $F$

## 6 Conclusions

This paper presented a topology optimization approach based on weak-form lower-bound yield design and second-order cone programming (SOCP) for the design of structures under plastic admissibility constraints. The proposed formulation combines density-based topology optimization with a plasticity-based stress decomposition, in which the stress field is separated into elastic and residual components to satisfy equilibrium and yield conditions. By reformulating the optimization problem into a set of second-order cone constraints, the present formulation enables efficient solution using convex optimization techniques while avoiding the need for nonlinear incremental elastoplastic analyses.

An exponential penalization strategy was introduced to suppress intermediate densities and generate clear black-and-white topologies. In addition, the formulation enables the use of conventional displacement-based finite elements, which efficiently simplify implementation and avoiding the complexity associated with stress- or mixed-based finite element formulations. Density filtering was further employed to improve numerical stability and reduce mesh dependence in the optimized solutions. The numerical results demonstrated that the proposed framework successfully captures physically meaningful load-transfer mechanisms, produces clear structural layouts, and generates stress distributions consistent with the plastic admissibility condition. The obtained topologies also showed good agreement with the existing results reported in the literature. Future work may focus on extending the formulation to 3D prob-

lems, more advanced yield criteria, and shakedown-based topology optimization.

**Funding**

This research is funded by Vietnam Ministry of Science and Technology under grant number: ĐTĐLCN.03/25.

**Conflict of Interest**

The author declares that there is no conflict of interest.

**Declaration of generative AI and AI-assisted technologies in the writing process**

During the preparation of this work the authors used Grammarly (professional version) in order to improve the readability and language of the manuscript. After using this tool, the authors reviewed and edited the content as needed and take full responsibility for the content of the published article.

**Ethics approval and Consent to participate**

Not applicable

**Data Availability and Replication of Results**

No data were used for the research described in this article. All the results presented in this work can be reproduced following the formulations and strategies presented in sections 3 and 4 of the manuscript, using the Mosek optimization package with academic licence.

## A Density filtering

A Gaussian density filter is employed to regularize the material distribution and reduce numerical instabilities. For each triangular element $e$, the centroid is computed as

$$\mathbf{x}_e^c = \frac{1}{3}\sum_{i=1}^{3}\mathbf{x}_{e_i} \tag{22}$$

where $\mathbf{x}_{e_i}$ are the nodal coordinates of element $e$. The element area is denoted by $A_e$. A local neighborhood $\mathcal{N}_e$ is defined for each element based on a prescribed filter radius

$$\mathcal{N}_e = \{j \mid d_{ej} \leq R\} \tag{23}$$

where

$$d_{ej} = \left\|\mathbf{x}_j^c - \mathbf{x}_e^c\right\|_2 \tag{24}$$

is the Euclidean distance between the centroids of elements $e$ and $j$, and

$$R = r_{\min}h \tag{25}$$

is the physical filter radius. Here, $r_{\min}$ is a dimensionless parameter and $h$ is the characteristic mesh size.

Within the neighborhood $\mathcal{N}_e$, the influence of each neighboring element is determined by a Gaussian weight

$$w_{ej} = \exp\left[-\frac{1}{2}\left(\frac{d_{ej}}{\sigma}\right)^2\right] \qquad \sigma = \frac{R}{2} \tag{26}$$

This weighting function assigns higher influence to closer elements and rapidly decreases with distance, ensuring a smooth spatial averaging.

The filtered density $\widetilde{\rho}_e$ is obtained as a normalized, area-weighted average of neighboring densities:

$$\widetilde{\rho}_e = \frac{\sum_{j\in\mathcal{N}_e} w_{ej}A_j\rho_j}{\sum_{j\in\mathcal{N}_e} w_{ej}A_j} \tag{27}$$

The inclusion of the element area $A_j$ ensures consistency for non-uniform meshes and improves robustness.

To maintain numerical stability and avoid degeneracy, the filtered density is projected onto a bounded interval:

$$\rho_e^F = \min\left(1, \max\left(\rho_{\min}, \widetilde{\rho}_e\right)\right) \tag{28}$$

where $\rho_{\min}$ is a small positive value (e.g., $10^{-6}$).

## References


Alcazar E, Russ JB, Paulino GH (2025) Polyplas: A python implementation of a topology optimization framework for plasticity with unstructured polygonal finite elements. Structural and Multidisciplinary Optimization 68(8):1–30, DOI 10.1007/s00158-025-04055-2

Amir O (2017) Stress-constrained continuum topology optimization: A new approach based on elasto-plasticity. Structural and Multidisciplinary Optimization 55(5):1797–1818, DOI 10.1007/s00158-016-1618-8

Bendsøe MP, Sigmund O (2004) Topology Optimization: Theory, Methods, and Applications, 2nd edn. Springer Berlin Heidelberg, DOI 10.1007/978-3-662-05086-6

Bruggi M (2008) On an alternative approach to stress constraints relaxation in topology optimization. Structural and Multidisciplinary Optimization 36(2):125–141, DOI 10.1007/s00158-007-0203-6

Cheng W, Zhang X, Hu T, Li J, Wang Y (2024) Stress-constrained topology optimization using the velocity field level set method. Computers & Structures 305:107577, DOI 10.1016/j.compstruc.2024.107577

Duysinx P, Bendsøe MP (1998) Topology optimization of continuum structures with local stress constraints. International Journal for Numerical Methods in Engineering 43(8):1453–1478, DOI https://doi.org/10.1002/(SICI)1097-0207(19981230)43:8%3C1453::AID-NME480%3E3.0.CO;2-2

Eschenauer HA, Olhoff N (2001) Topology optimization of continuum structures: A review. Applied Mechanics Reviews 54(4):331–390, DOI 10.1115/1.1388075

Hassani B, Hinton E (1999) Homogenization and Structural Topology Optimization: Theory, Practice and Software. Springer London, DOI 10.1007/978-1-4471-0891-7

Herfelt MA, Poulsen PN, Hoang LC (2019) Strength-based topology optimisation of plastic isotropic von mises materials. Structural and Multidisciplinary Optimization 59(3):893–906, DOI 10.1007/s00158-018-2108-y

Hoang VN, Nguyen-Xuan H (2026) Multiscale structural optimization using mmbs on a truss-based ground structure. Computer Methods in Applied Mechanics and Engineering 461:119162

Jahangiry HA, Gholhaki M, Naderpour H, Tavakkoli SM (2021) Isogeometric level set topology optimization for elastoplastic plane stress problems. International Journal of Mechanics and Materials in Design 17(4):947–967, DOI 10.1007/s10999-021-09562-w

Kammoun Z, Smaoui H (2014) A direct approach for continuous topology optimization subject to admissible loading. Comptes Rendus Mécanique 342(9):520–531, DOI 10.1016/j.crme.2014.06.003

Kuci E, Jansen M (2022) Level set topology optimization of elastoplastic materials with local stress constraints. Structural and Multidisciplinary Optimization 65(6):170, DOI 10.1007/s00158-022-03268-z

Kundu RD, Zhang XS (2023) Stress-based topology optimization for fiber composites with improved stiffness and strength: Integrating anisotropic and isotropic materials. Composite Structures 320:117041, DOI 10.1016/j.compstruct.2023.117041

Le C, Norato J, Bruns T, Ha C, Tortorelli D (2010) Stress-based topology optimization for continua. Structural and Multidisciplinary Optimization 41(4):605–620, DOI 10.1007/s00158-009-0440-y

Li L, Zhang G, Khandelwal K (2017) Design of energy dissipating elastoplastic structures under cyclic loads using topology optimization. Structural and Multidisciplinary Optimization 56(2):391–412, DOI 10.1007/s00158-017-1671-y

Luo YJ, Kang Z (2012) Topology optimization of continuum structures with drucker–prager yield stress constraints. Computers & Structures 90:65–75, DOI 10.1016/j.compstruc.2011.10.008

Luo YJ, Wang MY, Kang Z (2013) An enhanced aggregation method for topology optimization with local stress constraints. Computer Methods in Applied Mechanics and Engineering 254:31–41, DOI 10.1016/j.cma.2012.10.019

Maute K, Schwarz S, Ramm E (1998) Adaptive topology optimization of elastoplastic structures. Structural Optimization 15(2):81–91, DOI 10.1007/BF01278493

Mourad L, Bleyer J, Mesnil R, Suquet P (2021) Topology optimization of load-bearing capacity. Structural and Multidisciplinary Optimization 64(3):1367–1383, DOI 10.1007/s00158-021-02923-1

Sigmund O (2007) Morphology-based black and white filters for topology optimization. Structural and Multidisciplinary Optimization 33(4):401–424, DOI 10.1007/s00158-006-0087-x

Smaoui H, Kammoun Z (2022) Convergence of the direct limit analysis design method for discrete topology optimization. Optimization and Engineering 23:1–24, DOI 10.1007/s11081-021-09638-4

Wang C, Zhao Z, Zhou M, Sigmund O, Zhang XS, Zhu JH, Guo X, Du Z, Zhou S, Li Q (2021) A comprehensive review of educational articles on structural and multidisciplinary optimization. Structural and Multidisciplinary Optimization 64:2827–2880, DOI 10.1007/s00158-021-03050-7

Wang Y, Li X, Long K, Wei P (2023) Open-source codes of topology optimization: A summary for beginners to start their research. Computer Modeling in Engineering & Sciences 137(1):1–34, DOI 10.32604/cmes.2023.027603

Xia L, Breitkopf P (2017) Recent advances on topology optimization of multiscale nonlinear structures. Archives of Computational Methods in Engineering 24(2):227–249, DOI 10.1007/s11831-016-9170-7

Xu S, Liu J, Zou B, Li Q, Ma Y (2021) Stress constrained multi-material topology optimization with the ordered simp method. Computer Methods in Applied Mechanics and Engineering 373:113453, DOI 10.1016/j.cma.2020.113453

Zhang X, Li X, Zhang Y (2023) A framework for plasticity-based topology optimization of continuum structures. International Journal for Numerical Methods in Engineering 124(7):1493–1509, DOI 10.1002/nme.7172